RSC Advances

ROYAL SOCIETY OF CHEMISTRY

www.rsc.org/advances

Graphical abstract:

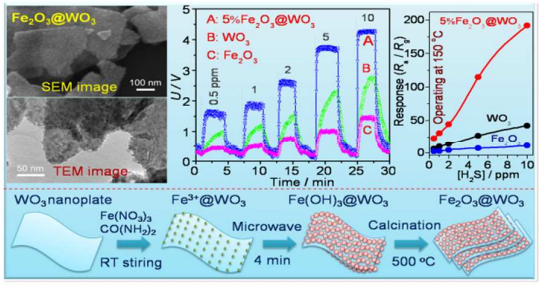

Text: $Fe_2O_3@WO_3$ composites with ultrahigh specific surface areas, synthesized via a simple microwave-assisted method, show high H_2S gas-sensing performance.

Hierarchical Fe_2O_3@WO_3 Nanostructures with Ultrahigh Specific Surface Areas: Microwave-Assisted Synthesis and Enhanced H_2S-Sensing Performance

Li Yin [a], Deliang Chen [a, *], Mengjie Feng [a], Lianfang Ge [a], Dewei Yang [a], Zhanhong Song [b], Bingbing Fan [a], Rui Zhang [a, c, *], Guosheng Shao [a, d]

[a] *School of Materials Science and Engineering, Zhengzhou University, 100 Science Road, Zhengzhou 450001, P.R.China*

[b] *Zhengzhou Foreign Language School, 6 Fengyang Street, Zhengzhou 450000, P.R.China*

[c] *Laboratory of Aeronautical Composites, Zhengzhou Institute of Aeronautical Industry Management, University Centre, Zhengdong New District, Zhengzhou 450046, China*

[d] *Institute for Renewable Energy and Environmental Technology, University of Bolton, Bolton BL3 5AB, UK*

***Corresponding author*:**

School of Materials Science and Engineering, Zhengzhou University, 100 Science Road, Zhengzhou 450001, P.R. China

E-mail address: dlchen@zzu.edu.cn (D.L. Chen) and zhangray@zzu.edu.cn (R. Zhang)

Tel: +86-371-67781046 Fax: +86-371-67781593

Abstract: Hierarchical Fe_2O_3@WO_3 nanocomposites with ultrahigh specific areas, consisting of Fe_2O_3 nanoparticles (NPs) and single-crystal WO_3 nanoplates, were synthesized via a microwave-heating (MH) in-situ growth process. WO_3 nanoplates were derived by an intercalation and topochemical-conversion route, and the Fe_2O_3 NPs were in-situ grown on the WO_3 surfaces via a heterogamous nucleation. The water-bath-heating (WH) process was also developed to synthesize Fe_2O_3@WO_3 nanocomposite for comparison purposes. The techniques of X-ray diffraction (XRD), X-ray photoelectron spectrum (XPS), scanning electron microscopy (SEM) and transmission electron microscopy (TEM) were used to characterize the samples obtained. The results show that α-Fe_2O_3 NPs with a size range of 5 – 10 nm are uniformly, tightly anchored on the surfaces of WO_3 nanoplates in the Fe_2O_3@WO_3 samples obtained via the MH process, whereas the α-Fe_2O_3 NPs are not uniform in particle-sizes and spatial distribution in the Fe_2O_3@WO_3 samples obtained via the WH process. The BET surface area of the 5wt.%Fe_2O_3@WO_3 sample derived by the MH process is as high as 1207 $m^2 g^{-1}$, 5.9 times higher than that (203 $m^2 g^{-1}$) of the corresponding WO_3 nanoplates. The dramatic enhancement in the specific surface area of the Fe_2O_3@WO_3 samples should be attributed to the hierarchical microstructure, which makes the internal surfaces or interfaces in aggregated polycrystals fully be outside surfaces via a house-of-cards configuration, where the single-layered and disconnected Fe_2O_3 NPs are tightly anchored on the surfaces of the WO_3 nanoplates. The gas-sensing properties of the Fe_2O_3@WO_3 sensors were investigated. The gas-sensors based on the Fe_2O_3@WO_3 obtained via the MH process show high response and selectivity to H_2S at low operating temperatures. The 5%Fe_2O_3@WO_3 sample shows the highest H_2S-sensing response at 150 ^oC. Its response to 10-ppm H_2S is as high as 192, 4 times higher than that of the WO_3-nanoplate sensor. The improvement in gas-sensing performance of the Fe_2O_3@WO_3 nanocomposites can be attributed to the synergistic effect in compositions and the hierarchical microstructures with ultrahigh specific surface areas.

1. Introduction

Metal oxide semiconductors (MOSs) have been extensively investigated for gas-sensing applications due to their unique electrical and optical properties.[1-3] The gas-sensing performance of a MOS sensor relies upon the interaction of the target gases with adsorbed oxygen on the oxide surface according to the related "electron depletion layer" models.[4] Yamazoe and Shimanoe[5,6] further formulated theoretical equations to account for the gas-sensing response and proposed a new type of "volume depletion", which indicated that decreasing the crystallite size and increasing the adsorbed oxygen can increase "volume depletion" and then improve gas performance. Thus, developing MOS nanocrystals with small particle sizes and higher specific surface areas is the frontier in gas-sensing material investigation. Recently, hierarchical functional nanocomposites with a tunable dimension and structure have become a research hotspot for its potential high surface area with promising applications in high-performance gas-sensors.[2,7,8] Particularly, the hierarchical binary oxide nanocomposites can provide high sensitivities and fast response due to the formation of electric junctions at the interface of the heterostructures and a more extended depletion layer.[9,10]

Tungsten trioxide (WO_3), an n-type semiconductor with band gaps of ~2.7 eV, has been extensively studied as gas-sensing materials because of its high response to various gases.[11-16] Several WO_3-based binary oxide composites such as WO_3/ZnO,[17] NiO/WO_3,[18] CuO/WO_3[19] and SnO_2/WO_3,[20] have been reported as high-performance gas sensors. The plate-like heterogeneous NiO/WO_3 nanocomposites were synthesized by annealing $Ni(OH)_2$ and H_2WO_4 nanoplates in air and their gas-sensing sensitivity towards NO_2 were enhanced due to their p–n heterogeneous characteristics.[18] Kida et al.[20] introduced SnO_2 nanoparticles into WO_3 lamella-based films obtained by mixing two suspensions containing $WO_3 \cdot nH_2O$ and SnO_2 nanoparticles, and the enhanced gas-sensing response is owe to the porosity improvement. But unfortunately, the control in microstructure and distribution of the second phase is always extremely difficult by the RF sputtering technique[19] or simply mixing their precursors.[18,20] As a result, the advantages of potential high surface areas cannot be fully embodied in practical applications. Simple and efficient methods are urgent for the

construction of WO_3-based binary oxide heterostructures. Recently, microwave-assisted techniques have been used to synthesize inorganic materials for the potentials in controlling microstructures and morphology due to the selective absorption of microwave energy.[21]

Hematite (α-Fe_2O_3), with a band gap of 2.0−2.2 eV, is suitable to implement a host/guest n/n junction architecture with WO_3.[22] The scaffold host material of WO_3 has a larger band gap than α-Fe_2O_3, and the conduction band of WO_3 is lower in energy than that of α-Fe_2O_3, allowing efficient electron transport across the host/guest interface. Fe_2O_3/WO_3 nanocomposites have been fabricated and used as nano-electrodes,[23] water splitting[22,24] and visible-light-driven photocatalysis.[25] The α-Fe_2O_3 nanocrystals has also been investigated as a promising gas-sensing material especially for H_2S detection.[26-31] Thus, the combination of WO_3 and α-Fe_2O_3 is expected to be an efficient gas-sensing system for H_2S-detection. However, to our best knowledge, the investigation on α-Fe_2O_3/WO_3 nanocomposites for gas-sensing application has not been reported to date.

In this paper, we develop a simple microwave-assisted process to fabricate uniform-distributed α-Fe_2O_3 nanoparticles (NPs) on WO_3 nanoplates, forming Fe_2O_3@WO_3 nanocomposites with ultrahigh surface areas that are highly sensitive to H_2S gas. The two-dimensional WO_3 nanoplates are synthesized via a robust intercalation and topochemical conversion route.[32] Furthermore, the as-obtained WO_3 nanoplates have a high diameter-to-thickness ratio and single-crystalline structure, which is suitable as an efficient substrate to construct hierarchical nanocomposites.[33] The Fe_2O_3 NPs are in-situ formed on the surfaces of WO_3 nanoplates via the microwave heating followed by calcination. Using the above WO_3 nanoplates as the substrate, the α-Fe_2O_3 NPs are uniform anchored on their surfaces to form hierarchical Fe_2O_3@WO_3 nanostructures. The hierarchical Fe_2O_3@WO_3 nanostructures not only prevent the aggregation of the α-Fe_2O_3 NPs, but also provide efficient diffusion paths and adsorption sites for gas molecules because of their ultrahigh surface areas.

The simple microwave heating process developed here offers several advantages: fast synthesis and no high pressure. The WO_3 nanoplate is kept stable during the fast synthesis by avoiding dissolution in alkaline conditions. In addition, the microwave process may promote the heterogeneous nucleation of $Fe(OH)_3$ NPs on the surfaces of WO_3 nanoplates due to selective absorption of microwave energy, leading to an uniformly distributed α-Fe_2O_3 NPs.

The gas-sensing properties of the as-obtained Fe_2O_3@WO_3 nanomaterials are comparatively evaluated with an emphasis on H_2S-sensing detection. The effects of α-Fe_2O_3 amounts, operating temperatures on H_2S-sensing properties, and the related mechanisms are carefully investigated.

2. Experimental section

2.1 Synthesis of WO_3 Nanoplates. WO_3 nanoplates were synthesized according to the literature with some modification.[32,34] Typically, tungstic acid (5.8 g, chemically pure) reacted with n-octylamine (50 ml, analytically pure) in heptane (350 mL, analytically pure) at room temperature for 72 h, forming tungstate-based inorganic-organic hybrid belts. The as-obtained hybrids were treated in a ~38% HNO_3 aqueous solution for 48 h to remove organic species, forming H_2WO_4 nanoplates. WO_3 nanoplates were finally obtained by calcining the above H_2WO_4 nanoplates at 400 ^oC for 2 h, and used as the supports for immobilizing α-Fe_2O_3 nanocrystals to construct hierarchical nanostructures.

2.2 Synthesis of hierarchical Fe_2O_3@WO_3 nanostructures. Fe_2O_3@WO_3 nanostructures were synthesized via two methods: the microwave heating (MH) process and the water-bath heating (WH) process. For the MH process, WO_3 nanoplates (0.1 g), $Fe(NO_3)_3 \cdot 9H_2O$ (0.025 g, analytically pure) and urea (0.01g, analytically pure) were mixed in 50 mL distilled water in a conical flask with an ultrasonic treating for ~2 h, and the as-obtained mixture was then placed in a microwave oven (500 W, 2.45 GHz) and heated for 4 min, followed by cooling treating in an ice bath. The brick-red solid particles were collected, washed and then dried in a vacuum oven at 60 ^oC for more than 12 h. Finally, the Fe_2O_3@WO_3 sample with a theoretical α-Fe_2O_3 content of 5 mass%, i.e., 5%Fe_2O_3@WO_3, was obtained by calcining the above precipitates in air at 500 ^oC for 3 h. The Fe_2O_3@WO_3 samples with various α-Fe_2O_3 contents, i.e., 2.5% Fe_2O_3@WO_3 and 9% Fe_2O_3@WO_3, were synthesized using the similar process, just changing the amounts of $Fe(NO_3)_3$ and urea. The molar ratio of urea to $Fe(NO_3)_3$ was kept ~2.6 for all of the samples. For the WH process, the mixture containing 0.1 g of WO_3 nanoplates, 0.025 g of $Fe(NO_3)_3 \cdot 9H_2O$ and 0.01g of urea was treated in a water bath at 85 ^oC for 3 h under a stirring condition. The precipitates, obtained by centrifugation, washing with distilled water and ethanol, and drying in a vacuum

oven at 60 °C for more than 12 h, were finally calcined at 500 °C for 3 h. The 5%Fe_2O_3@WO_3 nanocomposite was obtained through the water-bath heating process.

2.3 Synthesis of Fe_2O_3 nanocrystals. Pure Fe_2O_3 nanocrystals were synthesized via a hydrothermal process**.** Typically, $Fe(NO_3)_3 \cdot 9H_2O$ (0.25 g) and urea (0.1 g) were dissolved in 50 mL water and stirring for 30 min to form a transparent solution. After treated in the microwave oven for 4 min, the above mixture was transferred into a 100 ml Teflon lined stainless autoclave and maintained at 150 °C for 4 h. The resulting solid was collected, washed and dried at 60 °C for ~ 12 h. Finally, the α-Fe_2O_3 nanocrystals were obtained by calcining the above solid in air at 500 °C for 3 h.

2.4 Materials characterization. The phases of the samples were confirmed via X-ray diffraction (XRD) analysis by using a Rigaku D/Max-3B X-ray diffractometer with Cu Kα radiation (XRD, λ = 0.15406 nm). The morphology and microstructures were characterized on a scanning electron microscope (SEM, JEOL JSM-5600, Japan) with an acceleration voltage of 15 kV, and on a transmission electron microscope (TEM, FEI Tecnai-G2, USA) with an acceleration voltage of 200 kV. For SEM observation, the samples were coated with a thin Pt film. The Brunauer-Emmett-Teller (BET) surface areas were measured using a Quantachrome Nova2000 sorption analyzer. The X-ray photoelectron spectrum (XPS) spectra of the Fe_2O_3@WO_3 sample were recorded on a multipurpose X-ray photoelectron spectroscope (Kratos Amicus, Manchester, UK) with a microfocused monochromatic X-ray source of Al Kα, using adventitious carbon (C1s 284.8 eV) as the calibration reference.

2.5 Gas-sensing measurement. The details for the sensor fabrication and the gas-sensing testing process were similar to our previous report.[35] The sensors were fabricated using a brush-coating method. Simply, the samples consisting of Fe_2O_3@WO_3 nanostructures, WO_3 nanoplates or α-Fe_2O_3 nanocrystals were mixed with a small amount of water to form the corresponding pastes, which were then coated onto the surfaces of alumina microtubes to form continuous thin films. The as-obtained thin films were heated at 300 °C for 5 h in air before gas-sensing test. The gas-sensing properties of the as-obtained sensors were evaluated using a commercial WS-30A system equipped with a computer terminal. The testing system was placed in a ventilating cabinet with a large draught capacity. The target substances for gas-sensing evaluation were injected into the closed chamber using a micro-injector. The

harmful gases (*e.g.*, H_2S, CH_4, CO, H_2 and SO_2) and some common organic vapors (*e.g.*, methanol, ethanol, isopropanol, methanal, acetone and benzene) were chosen as the target substances to evaluate the gas-sensing performance of the Fe_2O_3@WO_3 sensors, with an emphasis on H_2S-sensing testing. The H_2S detection were operated at 100–250 °C with a H_2S concentration [H_2S] range of 0.5–10 ppm, whereas the other target substances with a concentration of 100 ppm were used the sensing gases (or vapors) operating at 150 °C.

A sensor (R) was connected with a standard resistor (R_0) in series, and the total voltage (U_0) applied on the sensor and standard resistor was fixed to 5 V. The WS-30A system measured the voltage (U) loaded on the standard resistor (R_0), and the resistance (R) of the Fe_2O_3-WO_3 sensor were calculated according to $R = (5\text{-}U)\bullet R_0 / U$.[12] The sensor response (S) of a sensor based on an n-type semiconductor was defined as $S = R_a / R_g$ for reducing gases and $S = R_g / R_a$ for oxidizing gases, where R_a and R_g were the resistances of the sensor in air and in target gas, respectively. The response (or recovery) time was defined as the time in which the sensor reached 90% of the saturated signal upon exposure to (or removing) the target gas.[33,35]

3. Results and discussion

3.1. Synthesis and Characterization. Hierarchical Fe_2O_3@WO_3 nanocomposites are synthesized via a microwave heating process (Scheme 1). Firstly, Fe^{3+} ions are absorbed on the surfaces of WO_3 nanoplates because of the electrostatic interaction between the Fe^{3+} ions and the hydroxyls of WO_3 nanoplates. Urea molecules, $CO(NH_2)_2$, are possibly enriched around the surfaces of WO_3 nanoplates due to the combination of Fe^{3+} ions with $–NH_2$ groups in urea molecules. It is known that the quick heat and non-thermal effects of microwave radiation. When microwave heating is conducted, many hot spots generated rapidly on the surface of WO_3 nanoplates due to their selective absorption of microwave energy. Urea molecules around the WO_3 nanoplates are hydrolyzed to generate a large amount of OH^- ions as the temperature increases to ~80 °C in a short time (i.e., 4 min). As a result, $Fe(OH)_3$ clusters are predominately formed on the surfaces of WO_3 nanoplates via a heterogeneous nucleation mechanism, and then grow up rapidly during the microwave heating. The $Fe(OH)_3$ nanocrystals are in situ formed and tightly immobilized on the surfaces of WO_3 nanoplates,

and the hierarchical $Fe(OH)_3@WO_3$ nanostructures can be expected. Hierarchical $Fe_2O_3@WO_3$ nanocomposites are then obtained by calcining the $Fe(OH)_3@WO_3$ at 500 ^oC for 3 h in air. On the basis of the above analysis of the reaction mixture, the possible reaction can be described as eqs.1-3.

$$CO(NH_2)_2+3H_2O \rightarrow 2NH_4^+ + 2OH^- + CO_2\uparrow \quad (1)$$

$$Fe^{3+}@plate\text{-}WO_3 + 3OH^- \rightarrow Fe(OH)_3@\ plate\text{-}WO_3 \quad (2)$$

$$2Fe(OH)_3@\ plate\text{-}WO_3 \rightarrow Fe_2O_3@\ plate\text{-}WO_3 + 3H_2O \quad (3)$$

Scheme 1.

Fig. 1 shows the typical XRD patterns of WO_3 nanoplates, α-Fe_2O_3 nanocrystals and 5%$Fe_2O_3@WO_3$ nanocomposite. Fig. 1a shows a XRD pattern of the pure Fe_2O_3 sample. The major peaks can be readily indexed to the (012), (104), (110), (113), (024), (116) and (214) reflections of the rhombohedral α-Fe_2O_3 phase (JCPDS card no. 33-0664). Fig. 1c shows a typical XRD pattern of the WO_3 nanoplates, and it can be readily indexed to a triclinic WO_3 phase according to the literature (JCPDS card no. 32-1395). Fig. 1b shows the XRD pattern of the 5%$Fe_2O_3@WO_3$ nanocomposite. The major peaks of the $Fe_2O_3@WO_3$ sample are similar to the those of WO_3 nanoplates, and the weak peak at around 33.1° in 2θ can correspond to the (104) plane of α-Fe_2O_3 phase. The weakened peaks of α-Fe_2O_3 phase in Fig. 1b are mainly because of the lower content of α-Fe_2O_3 in the $Fe_2O_3@WO_3$ nanocomposite.

Fig. 1.

The morphologies and microstructures of WO_3 nanoplates, Fe_2O_3 nanocrystals and 5%$Fe_2O_3@WO_3$ nanocomposite were characterized using SEM and TEM techniques. Fig. 2 shows the typical SEM and TEM images of the samples. Fig. 2a gives the SEM image of WO_3 nanoplates with dimensions of 100−700 nm in lateral size and 10−30 nm in thickness, which is similar to our precious report.[32] It needs to be noted that the surfaces of the pure WO_3 nanoplates are smooth, and the small particles are sparse. Fig. 2b shows the SEM image of α-Fe_2O_3 sample, and the pure α-Fe_2O_3 sample consists of particulate nanocrystals with a mean size of about 30 nm.

Fig. 2.

Fig. 2c shows a typical SEM image of the 5%$Fe_2O_3@WO_3$ sample. One can see that the α-Fe_2O_3 NPs with a mean size of about 9 nm are uniformly immobilized on the surfaces of

WO_3 nanoplates. Fig. 2d presents the energy dispersive X-ray spectroscopy (EDS) spectrum of the 5%Fe_2O_3@WO_3 nanocomposite, and the elements of W, Fe and O are detected in the sample. Fig. 2e show the typical low-magnification TEM image of the 5%Fe_2O_3@WO_3 nanostructure. One can further confirmed that the α-Fe_2O_3 NPs with a size range of 5−10 nm are uniformly and tightly immobilized on the surfaces of WO_3 nanoplates, similar to the SEM observation. Fig. 2f shows the high resolution TEM (HRTEM) image. The lattice fringes with a crystalline interplanar spacing of 0.376 nm can be attributed to the (020) plane of the WO_3 phase, and the lattice fringes with a crystalline interplanar spacing of 0.27 nm should be attributed to the (104) planes of the α-Fe_2O_3 phase. The corresponding two-dimensional fast Fourier transforms (FFT) of the lattice image given in the inset of Fig. 2f corroborate the co-existence of WO_3 and α-Fe_2O_3 phases. It should be emphasized that the α-Fe_2O_3 NPs are tightly anchored on the surfaces and edges of WO_3 nanoplates, and no discrete α-Fe_2O_3 NPs are found in the large TEM observation field. From the SEM and TEM images, one sees that the α-Fe_2O_3 NPs with very small sizes are not aggregated because of the support effect of WO_3 nanoplates, suggesting that the hierarchical nanostructures derived from zero-dimensional nanoparticle and two-dimensional nanoplates can be an ideal configuration to prevent the small nanoparticles from aggregation.

Fig. 3.

The microstructures of the Fe_2O_3@WO_3 composites were also characterized using the Brunauer-Emmett-Teller (BET) nitrogen sorption-desorption measurement. Fig. 3 shows the typical N_2 adsorption–desorption isotherms and the BJH pore-size distribution curves of the 5%Fe_2O_3@WO_3 composite and the support of WO_3 nanoplates. One can find both the WO_3 nanoplates (Fig. 3a) and the 5%Fe_2O_3@WO_3 composite (Fig. 3b) show a similar type II isotherm with no obvious hysteresis, and there are no obvious peaks in the pore-size distribution curves (insets in Fig. 3a and b). According to the above BET results, the WO_3 nanoplates and the 5%Fe_2O_3@WO_3 composite are of a non-porous structure.[36] The BET specific surface area of the WO_3 nanoplates is 203 $m^2 g^{-1}$, similar to our previous report.[32] The introduction of a small amount of α-Fe_2O_3 NPs on WO_3 nanoplates using the MH process highly enhances the BET specific surface areas. For example, the 5%Fe_2O_3@WO_3 composite has a BET specific surface area as high as 1207 $m^2 g^{-1}$, which is 5.9 times higher than that of

the corresponding WO_3 nanoplates. To the best of our knowledge, it is possibly the highest value in BET surface areas for a non-porous metal oxide material. Taking the SEM and TEM observations into account, the dramatic enhancement in the specific surface area of the Fe_2O_3@WO_3 samples should be attributed to the hierarchical microstructure, which makes the internal surfaces or interfaces in aggregated particles fully be outside surfaces via a house-of-cards configuration, where the single-layered and disconnected α-Fe_2O_3 NPs (several nanometers in size) are tightly anchored on the surfaces of the ultrathin WO_3 nanoplates.

Fig. 4.

Elemental compositions and chemical states of the hierarchical Fe_2O_3@WO_3 nanocomposites were analyzed using the XPS technique. Fig. 4 shows the typical XPS spectra of the 5%Fe_2O_3@WO_3 nanocomposite. A survey spectrum shown in Fig. 4a confirms that there are 4 elements of W, Fe, O and C detected. The elements of W, Fe and O should belong to the Fe_2O_3@WO_3 sample, and the C species is due to the carbon tape used to attach the sample powders during the XPS measurement. Fig. 4b shows the W 4f spectrum, which has two peaks at 35.4 eV and 37.5 eV, corresponding to the $W4f_{7/2}$ and $W4f_{5/2}$ of the crystalline WO_3 species, respectively.[28] Fig. 4c shows the Fe 2p spectrum, and there are two peaks at 711.2 and 725.3 eV, belonging to Fe $2p_{3/2}$ and Fe $2p_{1/2}$ of α-Fe_2O_3, respectively.[37] The O 1s spectrum in Fig. 4d shows a wide peak with a large hump on the high-energy side, and the wide peak can be fitted to be three sub-peaks at 530.4, 532.2 and 533.4 eV. The intense peak at 530.4 eV can be assigned to the lattice oxygen in the crystalline WO_3 and α-Fe_2O_3 species. The peak at 532.2 eV may be due to the oxygen ions (O_2^-, O^- and O^{2-}) adsorbed on the surfaces of the hierarchical Fe_2O_3@WO_3 nanostructure, whereas the peak at 533.4 eV is usually ascribed to the adsorbed H_2O molecules.[38,39] The intense intensities of the O 1s XPS peaks at 532.2 and 533.4 eV suggest that there is a large amount of adsorbed oxygen and H_2O molecules on the surfaces of the Fe_2O_3@WO_3 nanocomposite because of its ultrahigh BET specific surface area (1207 $m^2 g^{-1}$).

Fig. 5.

Efficient control in particle sizes and location distribution of a second phase is very important in the construction of hierarchical nanostructures. In the present Fe_2O_3@WO_3

system synthesized via the MH process, the particle sizes and number density of the α-Fe_2O_3 NPs anchored on the surfaces of WO_3 nanoplates can be readily adjusted by changing the Fe-ion concentration in the precursors, i.e., by changing the contents of α-Fe_2O_3 in the Fe_2O_3@WO_3 composites. The typical SEM images of the 2.5%Fe_2O_3@WO_3 and 9%Fe_2O_3@WO_3 composites are shown in Fig. 5a and b, respectively. One can see clearly that the number densities of α-Fe_2O_3 NPs in 5% Fe_2O_3@WO_3 (Fig. 2c) and 9% Fe_2O_3@WO_3 composites (Fig. 5b) are higher than that of the 2.5%Fe_2O_3@WO_3 composite (Fig. 5a). The particle sizes of the α-Fe_2O_3 NPs in the Fe_2O_3@WO_3 composites are statistically analyzed according to the SEM observations (Fig. 5a, 2c and 5b) are shown in Fig. 5c. The mean particle size of the α-Fe_2O_3 NPs in the Fe_2O_3@WO_3 nanocomposites increases from ~9 nm to ~13 nm when the apparent content of Fe_2O_3 NPs increases from 2.5% to 9%. It should be noted that the particle sizes of the α-Fe_2O_3 NPs measured according to the SEM images are a little larger than those (~5 nm) observed in the TEM images (Fig. 2e and f). The possible reason should be the Pt-coating during the preparation of SEM samples.

Fig. 6.

To demonstrate the efficiency and advantages of the microwave heating (MH) process in the construction of hierarchical nanostructures, we comparatively developed a water-bath heating (WH) process to synthesize the Fe_2O_3@WO_3 composites using the similar synthetic parameters except the heating manner. As a typical example, Fig. 6a shows the SEM image of the 5%Fe_2O_3@WO_3 composite obtained via the WH process at 85 ^oC for 3 h. One can find that most of the α-Fe_2O_3 NPs are loosely attached on the surfaces of WO_3 nanoplates, and the location distribution is random and uneven in Fig. 6a. In addition, many dissociative α-Fe_2O_3 NPs with aggregated structures can be found during the SEM observation (Fig. 6a). Comparatively, the 5%Fe_2O_3@WO_3 composite obtained via the MH process consists of monodispersed α-Fe_2O_3 NPs tightly anchored on the WO_3 nanoplates evenly, and few dissociative α-Fe_2O_3 NPs can be find in the SEM observation. We therefore infer that in the MH process the α-Fe_2O_3 NPs are in-situ grown on the WO_3 nanoplates via the heterogeneous nucleation mechanism, whereas in the WH process, the α-Fe_2O_3 NPs are firstly formed mainly via a homogenous nucleation mechanism, and then loosely adsorbed on the surfaces of WO_3 nanoplates. The above inference can also be corroborated by the experimental

phenomena: the filtrates are colorless in the MH process, whereas they are light brick-red in the WH process. The light brick-red suspension should be discrete $Fe(OH)_3$ clusters, which then turn to be α-Fe_2O_3 NPs by calcination.

The advantages of the MH process in the synthesis of hierarchical nanostructures are obvious when compared with the WH process. Firstly, the second-phase nanocrystals can be tightly anchored on the supports via the in-situ heterogeneous nucleation growth because the high-efficient microwave energy can be selectively reacted with the precursor system. Secondly, the MH process is much rapider than the WH process in the synthesis of hierarchical nanostructures. For example, the synthesis of 5%Fe_2O_3@WO_3 nanocomposite requires more than 3 h in the WH process, but just 4 min in the MH process. In addition, as the N_2 adsorption–desorption isotherms shown in Fig. 6b, the BET specific surface area of the 5%Fe_2O_3@WO_3 composite obtained via the WH process is 300 $m^2 g^{-1}$, which is far below that (1207 $m^2 g^{-1}$) of the 5%Fe_2O_3@WO_3 composite obtained via the MH process.

3.2. Gas-sensing performance. Hierarchical metal oxide nanocomposites with high specific surface areas are promising in developing high-performance gas-sensors. The Fe_2O_3@WO_3 nanocomposites obtained via the MH process are thus used as the active materials to detect harmful and combustible substances. Fig. 7 shows the typical H_2S-sensing properties of the Fe_2O_3@WO_3 nanocomposites, being compared with the WO_3 nanoplates and α-Fe_2O_3 nanoparticles obtained by a hydrothermal method. Fig. 7a shows the typical H_2S-sensing (U–t) profiles of the sensors operating at 150 ^oC upon exposure to H_2S gases with a concentration range of 0.5–10 ppm. The U–t curves show the change in voltage (U) loaded on the standard resistor as a function of the time (t) when the target gas are injected and discharged. One can see that the U values sharply rise and drop when the H_2S gas are injected and discharged for the sensors derived from the Fe_2O_3@WO_3 nanocomposites under the testing conditions, indicating that the Fe_2O_3@WO_3 sensors are highly sensitive to low-concentration H_2S gases and their resistances decrease quickly upon exposure to H_2S gases. Comparatively, the responses of the sensors derived from the pure WO_3 nanoplates and the α-Fe_2O_3 nanoparticles are relatively weak. The response details upon exposure to a 10 ppm H_2S gas are shown in Fig. 7b. One can see that the Fe_2O_3@WO_3 nanocomposites with

various amounts (2.5-9 wt.%) of α-Fe_2O_3 NPs show much faster and higher response than WO_3 nanoplates and Fe_2O_3 nanoparticles. Fig. 7c shows the plots of the response (R_a / R_g) of the sensors versus the concentration of H_2S gases ([H_2S] / ppm). The responses of all the sensors increase with the increases of [H_2S]. For a given [H_2S] value, the sensitivity in a descending order is 5%Fe_2O_3@WO_3 > 2.5%Fe_2O_3@WO_3 > 9%Fe_2O_3@WO_3 > WO_3 > α-Fe_2O_3. Typically, the response of the 5%Fe_2O_3@WO_3 sensor upon exposure to a 10-ppm-H_2S gas is as high as 192, up to 4-fold that (43) of the WO_3-nanoplate sensor and 17-fold that (11) of the α-Fe_2O_3-nanoparticle sensor. For a given [H_2S] value, the responses of the Fe_2O_3@WO_3 sensors increase firstly and then decrease with the increase of the α-Fe_2O_3 amounts, and the optimal amount of α-Fe_2O_3 is about 5wt.% under the present test condition.

Fig. 7.

Operating temperature usually highly influences the response of a gas sensor based on metal oxide semiconductors. Fig. 7d shows the typical responses of the sensors derived from the WO_3 nanoplates, α-Fe_2O_3 nanoparticles and 5%Fe_2O_3@WO_3 nanocomposite upon exposure to 5 ppm H_2S operating at different temperatures (i.e., 100 – 250 °C). Both the WO_3 and Fe_2O_3@WO_3 sensors have a maximum response at around 150 °C, and their responses are 27 and 115, respectively. The response changes of the 5%Fe_2O_3@WO_3 sensor are much larger than those of the WO_3-nanoplate sensor from 100 to 250 °C. For the α-Fe_2O_3-nanoparticle sensor, the responses are less than 10 at the operating-temperature range of 100 – 250 °C.

Fig. 8.

The response and recovery times, embodying the response speeds, are important parameters in evaluating the performance of a gas-sensor. Fig. 8 shows the response and recovery times of the sensors derived from the WO_3 nanoplates and 5%Fe_2O_3@WO_3 nanocomposite upon exposure to 5-ppm H_2S operating at 100–250 °C. One can see that a higher operating temperature is helpful to shorten the response and recovery times, and that the 5%Fe_2O_3@WO_3 sensor has shorter response and recovery times than the WO_3 sensor. Operating at 100 °C, the response and recovery times of the 5%Fe_2O_3@WO_3 sensor are 17 s and 150 s, respectively (Fig. 8b), much shorter than those (239 s and 560 s) of the WO_3 sensor (Fig. 8a). When the operating temperature is higher than 150 °C, the response time of the 5%Fe_2O_3@WO_3 sensor is as short as 3 – 9 s, and its recovery time is about 10 – 38 s. The

rapid response of the Fe_2O_3@WO_3 sensors should be attributed to the hierarchical nanostructure and ultrahigh specific surface areas, providing efficient diffusion paths and adsorption sites for gas molecules.

The selective response of a gas sensor is also important in practical applications. Fig. 9 shows the selectivity of the sensors based on the WO_3 nanoplates and 5%Fe_2O_3@WO_3 nanocomposite operating at 150 ^oC. Various gases and organic vapors, including CH_4, CO, H_2, SO_2, methanol, ethanol, isopropanol, methanal, acetone and benzene, with apparent concentrations of 100 ppm, are used as target substances to evaluate the selective response performance, comparing with 2 ppm H_2S. One can see that the WO_3-based sensors have the highest responses to 2-ppm H_2S, and the responses are less than 10 upon exposure to the other substances. The 5%Fe_2O_3@WO_3 sensor has a higher selectivity than the WO_3-nanoplate sensor under the same test conditions. The hierarchical Fe_2O_3@WO_3 nanocomposites are therefore suitable for H_2S detection at low operation temperatures (e.g., ~150 ^oC) due to its high response and selectivity to H_2S.

Fig. 9.

To demonstrate the advantages of the microwave-heating process, we compare the H_2S response of the 5%Fe_2O_3@WO_3 nanocomposites obtained by microwave-heating process (5%Fe_2O_3@WO_3-MH) and water-heating process (5%Fe_2O_3@WO_3-WH). Fig. 10 shows the typical responses of the 5%Fe_2O_3@WO_3-MH and 5%Fe_2O_3@WO_3-WH sensors operating at 150 ^oC upon exposure to H_2S gases with various concentrations (0.5-10 ppm). It is clear that the Fe_2O_3 NPs highly enhance the H_2S-sensing performance of WO_3 nanoplates, and that the microwave-heating process is more favorable in forming higher H_2S-sensing Fe_2O_3@WO_3 nanocomposites than the water-heating process. The possible reasons for the enhancement of the MH-process are its efficient control in more uniform distribution and smaller particle sizes of Fe_2O_3 NPs anchored on the surfaces of WO_3 nanoplates, resulting in ultrahigh specific surface areas of the Fe_2O_3@WO_3-MH samples.

Fig. 10.

3.3 Possible H_2S-sensing mechanism. The hierarchical Fe_2O_3@WO_3 nanocomposites obtained via the MH process with α-Fe_2O_3 NPs uniformly immobilized on the surfaces of

WO_3 nanoplates have a high specific surface area (1207 $m^2 g^{-1}$). the H_2S gas-sensing performance of the sensors derived from the Fe_2O_3@WO_3 nanocomposite has been greatly improved, and they show high response, high selectivity and rapid response.

Fig. 11.

The gas-sensing performance of n-type semiconductors of WO_3 and α-Fe_2O_3 nanocrystals relies upon the interaction of the target gases with adsorbed oxygen species. In air, oxygen molecules are adsorbed onto the surfaces of the α-Fe_2O_3 NPs and WO_3 nanoplates, and are then transferred to O^-, O^{2-}or O_2^- ions by trapping electrons from the conductive bands of the n-type oxides (α-Fe_2O_3 and WO_3), forming electron depletion layers with a high resistance (Fig. 11A). When the Fe_2O_3@WO_3 sensors are exposed to H_2S gas, the H_2S molecules react with the chemisorbed oxygen species (eqs. 4-5), releasing electrons back to the conduction bands of α-Fe_2O_3 and WO_3 (Fig. 11B). As a result, the concentration of electrons on the surface of the Fe_2O_3@WO_3 nanocomposites increases and the electron depletion layers decrease, forming a low-resistance state.

$$H_2S + 3O^-(ads) \rightarrow H_2O + SO_2 + 3e^- \quad (4)$$

$$H_2S + 3O^{2-}(ads) \rightarrow H_2O + SO_2 + 6e^- \quad (5)$$

As the operating temperature increases, high response is achieved because of the activation of adsorbed molecular oxygen and lattice oxygen (Fig. 11A). This phenomenon continues up to a certain optimum temperature, beyond which exothermic gas adsorption becomes difficult and gas molecules begin to desorb in large quantities, leading to a drop in sensor response.[40] Thus, the optimum temperature is a balance point between the above two conflicting aspects (i.e., activation and desorption).

The synergistic effect of WO_3 nanoplates and α-Fe_2O_3 NPs is the key factor improving the H_2S-sensing performances of the Fe_2O_3@WO_3 sensors. The additional depletion layers enhance the "volume depletion" because the Fe_2O_3@WO_3 nanocomposites have ultrahigh specific surface areas (i.e., 1207 $m^2 g^{-1}$ for the 5%Fe_2O_3@WO_3 sample), which allow them to absorb more gas molecules.[6] Additionally, the highly monolayer-dispersed Fe_2O_3 NPs on the surfaces of WO_3 nanoplates provides efficient and rapid electron-exchange between the cations: Fe(III) $\leftrightarrow$ Fe(II).[41] All the above aspects can improve the gas-sensing performance of the Fe_2O_3@WO_3 sensors. Although the exact mechanism for understanding the enhancement

in H_2S-sensing process is not available, the synergistic effect of the α-Fe_2O_3 and WO_3 species, not only in chemical compositions but also in microstructures, should be the essential origin to improve the low-temperature gas-sensing property of the WO_3-based materials.

4. Conclusions

Hierarchical Fe_2O_3@WO_3 nanocomposites have been fabricated via a simple microwave-heating process by in-situ growing α-Fe_2O_3 NPs on the surfaces of WO_3 nanoplates. The α-Fe_2O_3 NPs with particle sizes of 5-10 nm are uniformly, tightly anchored on the surfaces of WO_3 nanoplates. The BET specific surface area of the 5%Fe_2O_3@WO_3 composite is up to 1207 m^2 g^{-1}, 5.9 times higher than that of the WO_3 nanoplates. The Fe_2O_3@WO_3 nanocomposites are particularly sensitive and selective toward H_2S gas. The 5%Fe_2O_3@WO_3 sensor shows the highest H_2S-sensing property at the optimum operating temperature of 150 ^oC, and its sensitivity upon exposure to a10-ppm-H_2S gas is as high as 192, 4 times higher than that of the WO_3 nanoplates. The improved low-temperature gas-sensing performance ought to be attributed to the synergistic effect of the α-Fe_2O_3 and WO_3 species in chemical compositions and microstructures. The hierarchical nanostructures consisting of zero-dimensional nanoparticles on two-dimensional ultrathin nanoplates and the microwave-heating process developed in this work provide a simple and robust strategy to achieve high-performance gas-sensing materials.

Acknowledgments

This work was partly sponsored by National Natural Science Foundation of China (51172211, 512101207, 51172213), China Postdoctoral Science Foundation (2013M531682, 2014T70682), Foundation for University Young Key Teacher by Henan Province (2011GGJS-001), Program for Science & Technology Innovation Talents in Universities of Henan Province (14HASTIT011), Special Support Program for High-End Talents of Zhengzhou University (ZDGD13001), and Technology Foundation for Selected Overseas Chinese Scholar (Ministry of Human Resources and Social Security). Prof. D. Chen thanks Prof. Bing Zhang (Zhengzhou University) for his kind help in measuring BET surface area.

References

1 M.M. Arafat, B. Dinan, S.A. Akbar, A.S.M.A. Haseeb, *Sensors*, 2012, **12**, 7207-7258.

2 C.X. Wang, L.W. Yin, L.Y. Zhang, D. Xiang, R. Gao, *Sensors*, 2010, **10**, 2088-2106.

3 Y. Wang, S. Wang, H. Zhang, X. Gao, J. Yang, L. Wang, *J. Mater. Chem. A,* 2014, **2**, 7935-7943.

4 K. Wetchakun, T. Samerjai, N. Tamaekong, C. Liewhiran, C. Siriwong, V. Kruefu, A. Wisitsoraat, A. Tuantranont, S. Phanichphant, *Sens. Actuators, B,* **2011,** *160*, 580-591.

5 N. Yamazoe, K. Shimanoe, *J. Electrochem. Soc.,* 2008**, 155**, 85-92.

6 N. Yamazoe, K. Shimanoe, *J. Electrochem. Soc.,* 2008**, 155**,93-98.

7 J.H. Lee, *Sens. Actuators, B,* 2009**, 140**, 319-336.

8 A. Gurlo, *Nanoscale*, 2011, **3**, 154-165.

9 K. Potje-Kamloth, *Chem. Rev.,* 2008**, 108**, 367-399.

10 D. Bekermann, A. Gasparotto, D. Barreca, C. Maccato, E. Comini, C. Sada, G. Sberveglieri, A. Devi, R.A. Fischer, *ACS Appl. Mater. Interfaces,* 2012**, 4**, 928-934.

11 B. Cao, J. Chen, X. Tang, W. Zhou, *J. Mater. Chem.,* 2009**, 19**, 2323-2327.

12 D. Chen, X. Hou, T. Li, L. Yin, B. Fan, H. Wang, X. Li, H. Xu, H. Lu, R. Zhang, J. Sun, *Sens. Actuators, B,* 2011, **153**, 373-381.

13 T. Stoycheva, F.E. Annanouch, I. Gràcia, E. Llobet, C. Blackman, X. Correig, S. Vallejos, *Sens. Actuators, B,* 2014, **198**, 210-218.

14 C.S. Rout, M. Hegde, C.N.R. Rao, *Sens. Actuators, B,* 2008, **128**, 488-493.

15 J. Xiao, P. Liu, Y. Liang, H.B. Li, G.W. Yang, *Nanoscale*, 2012, **4**, 7078-7083.

16 S. Bai, K. Zhang, J. Sun, D. Zhang, R. Luo, D. Li, C. Liu, *Sens. Actuators, B,* 2014, **197**, 142-148.

17 S. An, S. Park, H. Ko, C. Lee, *Appl. Phys. A-Mater. Sci. Process,* 2012**, 108**, 53-58.

18 M. Bao, Y. Chen, F. Li, J. Ma, T. Lv, Y. Tang, L. Chen, Z. Xu, T. Wang, *Nanoscale,* 2014**, 6**, 4063-4066.

19 N.S. Ramgir, C.P. Goyal, P.K. Sharma, U.K. Goutam, S. Bhattacharya, N. Datta, M. Kaur, A.K. Debnath, D.K. Aswal, S.K. Gupta, *Sens. Actuators, B,* 2013**, 188**, 525-532.

20 T. Kida, A. Nishiyama, Z. Hua, K. Suematsu, M. Yuasa, K. Shimanoe, *Langmuir,* 2014**, 30**, 2571-2579.

21 Y.-J. Zhu, F. Chen, *Chem. Rev.,* 2014**, 114**, 6462-6555.

22 K. Sivula, F.L. Formal, M. Grätzel, *Chem. Mater.,* 2009**, 21**, 2862-2867.

23 W. Luo, T. Yu, Y. Wang, Z. Li, J. Ye, Z. Zou, *J.Phys. D: Appl. Phys.,* 2007**, 40**, 1091.

24 T. Jin, P. Diao, Q. Wu, D. Xu, D. Hu, Y. Xie, M. Zhang, *Appl. Catal. B: Environ.,* 2014**, 148–149**, 304-310.

25 S. Bai, K. Zhang, J. Sun, R. Luo, D. Li, A. Chen, *CrystEngComm,* 2014, **16**, 3289-3295.

26 Y. Wang, J. Cao, S. Wang, X. Guo, J. Zhang, H. Xia, S. Zhang, S. Wu, *J. Phys. Chem. C,* 2008**, 112**, 17804-17808.

27 V. Balouria, A. Kumar, S. Samanta, A. Singh, A.K. Debnath, A. Mahajan, R.K. Bedi, D.K. Aswal, S.K. Gupta, *Sens. Actuators, B,* 2013**, 181** , 471-478.

28 C. Zhao, W. Hu, Z. Zhang, J. Zhou, X. Pan, E. Xie, *Sens. Actuators, B,* 2014**, 195**, 486-493.

29 P. Sun, Y. Cai, S. Du, X. Xu, L. You, J. Ma, F. Liu, X. Liang, Y. Sun, G. Lu, *Sens. Actuators, B,* 2013**, 182**, 336-343.

30 Y. Wang, S. Wang, Y. Zhao, B. Zhu, F. Kong, D. Wang, S. Wu, W. Huang, S. Zhang, *Sens. Actuators, B,* 2007**, 125**, 79-84.

31 J. Ma, L. Mei, Y. Chen, Q. Li, T. Wang, Z. Xu, X. Duan, W. Zheng, *Nanoscale*, 2013, **5**, 895-898.

32 D. Chen, L. Gao, A. Yasumori, K. Kuroda, Y. Sugahara, *Small,* 2008**, 4**, 1813-1822.

33 D. Chen, L. Yin, L. Ge, B. Fan, R. Zhang, J. Sun, G. Shao, *Sens. Actuators, B,* 2013**, 185**, 445-455.

34 D. Chen, Y. Sugahara, *Chem.Mater.,* 2007**, 19**, 1808-1815.

35 D. Chen, X. Hou, H. Wen, Y. Wang, H. Wang, X. Li, R. Zhang, H. Lu, H. Xu, S. Guan, J. Sun, L. Gao, *Nanotechnology,* 2010**, 21**, 035501.

36 K.S.W. Sing, D. H. Everett, R.A.W. Haul, L. Moscou, R.A. Pierotti, J. Rouquerol,, T. Siemieniewska, *Pure & Appl. Chem.,* 1985**, 57**, 603-619.

37 Y.-J. Chen, X.-M. Gao, X.-P. Di, Q.-Y. Ouyang, P. Gao, L.-H. Qi, C.-Y. Li, C.-L. Zhu, *ACS Appl. Mater. Interfaces,* 2013**, 5**, 3267-3274.

38 A.F. Carley, M.W. Roberts, A.K. Santra, *J. Phys. Chem.B,* 1997**, 101**, 9978-9983.

39 J. Deng, L. Zhang, H. Dai, H. He, C.T. Au, *Ind. Eng. Chem. Res.,* 2008**, 47**, 8175-8183.

40 Z. Li, X. Lai, H. Wang, D. Mao, C. Xing, D. Wang, *J. Phys. Chem. C,* 2009**, 113**, 2792-2797.

41 L.A. Patil, M.D. Shinde, A.R. Bari, V.V. Deo, D.M. Patil, M.P. Kaushik, *Sens. Actuators, B,* 2011**, 155**, 174-182.

List of Fig. Captions

Scheme 1. Schematic illustration of the microwave-heating (MH) synthesis of the hierarchical Fe_2O_3@WO_3 nanocomposites with ultrahigh specific surface areas.

Fig. 1. Typical XRD patterns of (a) α-Fe_2O_3 nanoparticles obtained by the hydrothermal process, (b) 5%Fe_2O_3@WO_3 nanocomposite obtained by the MH process, and (c) WO_3 nanoplates.

Fig. 2. (a–c) Typical SEM images of (a) WO_3 nanoplates, (b) α-Fe_2O_3 nanoparticles and (c) 5%Fe_2O_3@WO_3 nanocomposites via the microwave-heating process; (d) EDS spectrum of the 5%Fe_2O_3@WO_3 nanocomposite (the inset is the corresponding SEM image); (e–f) TEM observation of the 5%Fe_2O_3@WO_3 nanocomposite: (e) low-magnification TEM image and (f) high-resolution TEM image (the inset is the corresponding FFT pattern).

Fig. 3. Nitrogen (N_2) adsorption–desorption isotherms of (a) WO_3 nanoplates and (b) 5%Fe_2O_3@WO_3 nanocomposites obtained by the microwave-heating process. The insets are their corresponding BJH pore-size distribution curves.

Fig. 4. XPS spectra of the 5%Fe_2O_3@WO_3 nanocomposite obtained by microwave-heating process: (a) a survey scan, (b) W 4f, (c) Fe 2p and (d) O1s.

Fig. 5. (a–b) Typical SEM images of (a) 2.5%Fe_2O_3@WO_3 and (b) 9%Fe_2O_3@WO_3 nanocomposites synthesized via the microwave-heating process. (c) The sizes of the α-Fe_2O_3 NPs immobilized on the surfaces of WO_3 nanoplates according to the statistical analysis of the SEM observations.

Fig. 6. (a) Typical SEM image and (b) N_2 adsorption–desorption isotherms of the 5%Fe_2O_3/WO_3 nanocomposite obtained via the water-heating (WH) process at 85 ^oC for 3 h.

Fig. 7. (a–b) Typical *U-t* response profiles of the Fe_2O_3@WO_3 (WH) nanocomposite operating at 150 ^oC upon exposure to H_2S gases with various concentrations: 0.5-10 ppm (a) and 10 ppm (b); (c) the plots of the [H_2S]-dependent responses of

the WO_3-based sensors operating at 150 ^oC (A: 5%Fe_2O_3@WO_3, B: 2.5%Fe_2O_3@WO_3, C: 9%Fe_2O_3@WO_3, D: WO_3, E: α-Fe_2O_3). (d) The operating-temperature-dependent responses of the sensors derived from WO_3, 5%Fe_2O_3@WO_3 and α-Fe_2O_3 upon exposure to 5-ppm H_2S.

Fig. 8. Response times and recovery times of the sensors derived from (a) WO_3 nanoplates and (b) 5%Fe_2O_3@WO_3 (MH) nanocomposite upon exposure to 5-ppm H_2S at an operating temperature range of 100–250 ^oC.

Fig. 9. Selective response at 150 ^oC of the sensors derived from the WO_3 nanoplates and 5%Fe_2O_3@WO_3 composite obtained by microwave-heating process.

Fig. 10. The plots of the [H_2S]-dependent responses of the WO_3, 5%Fe_2O_3@WO_3-MH and 5%Fe_2O_3@WO_3-WH sensors operating at 150 ^oC upon exposure to H_2S gases with various concentrations (0.5-10 ppm).

Fig. 11. A schematic demonstration of the adsorption and reaction process of O_2 and H_2S molecules at the interface of the hierarchical Fe_2O_3@WO_3 nanocomposite.

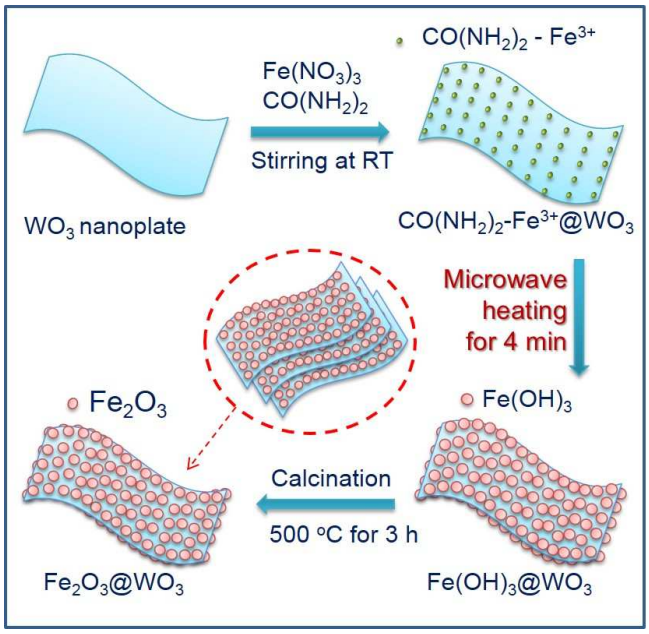

Scheme 1. By L. Yin, D. Chen, and *et al*..

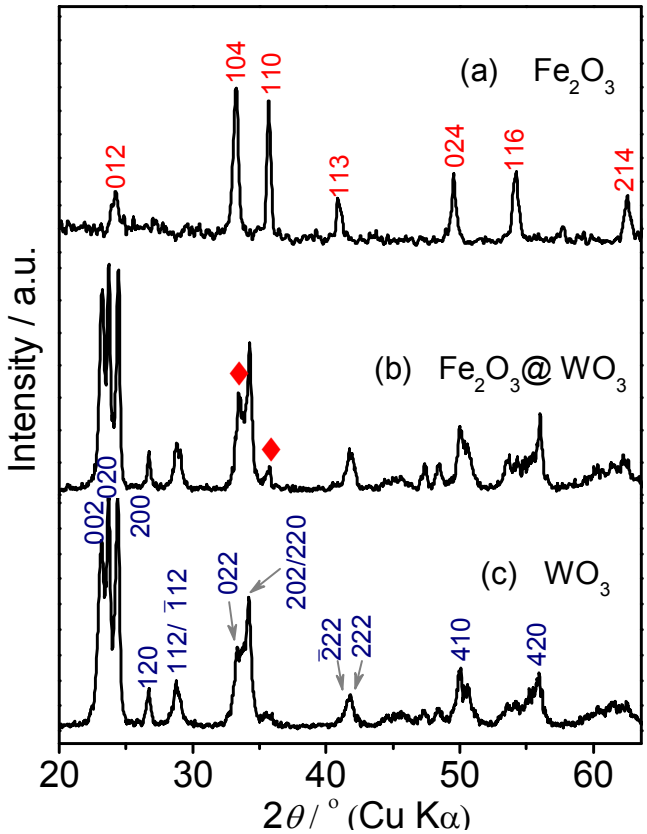

Fig. 1. By L. Yin, D. Chen, and *et al.*.

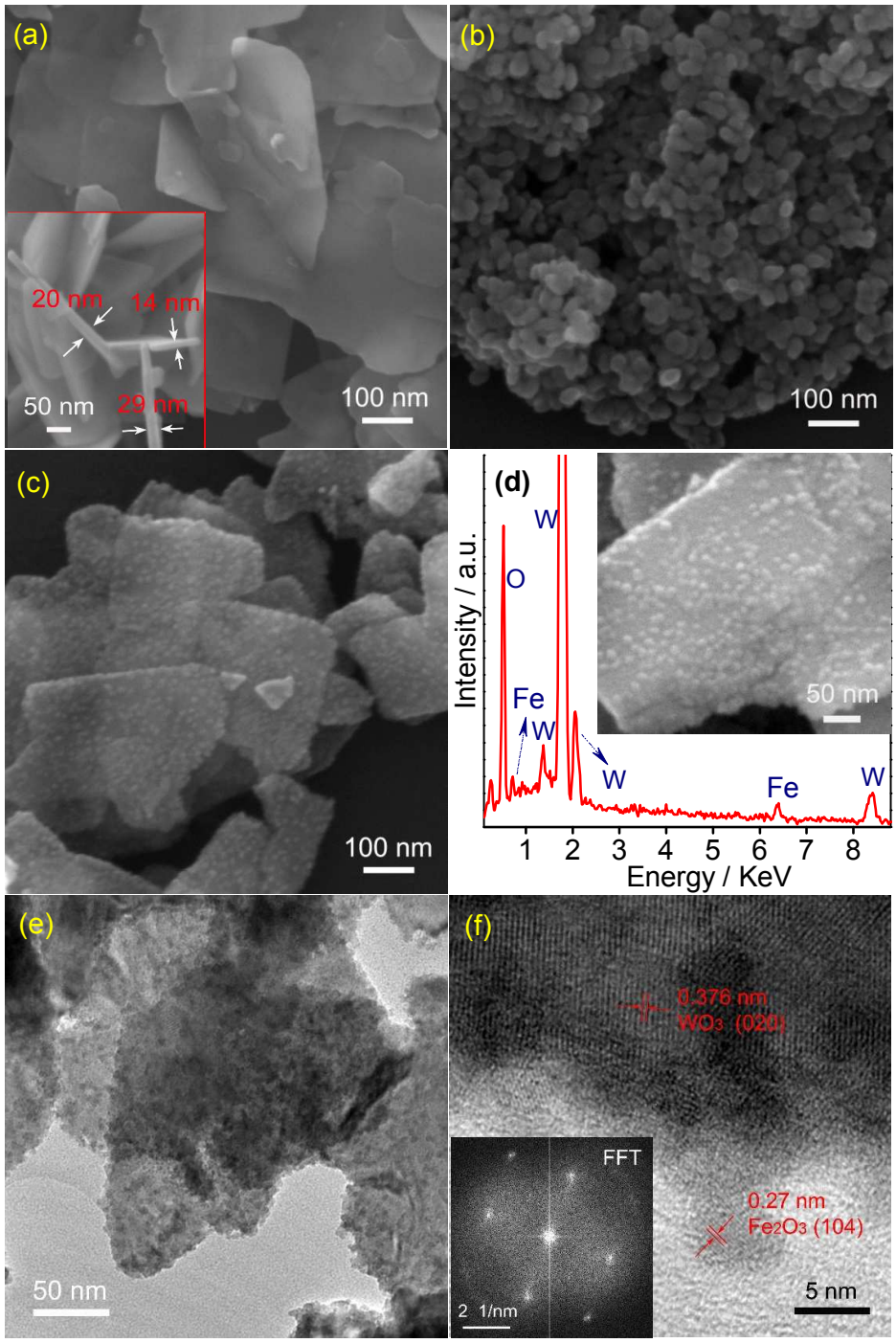

Fig. 2. By L. Yin, D. Chen, and *et al.*.

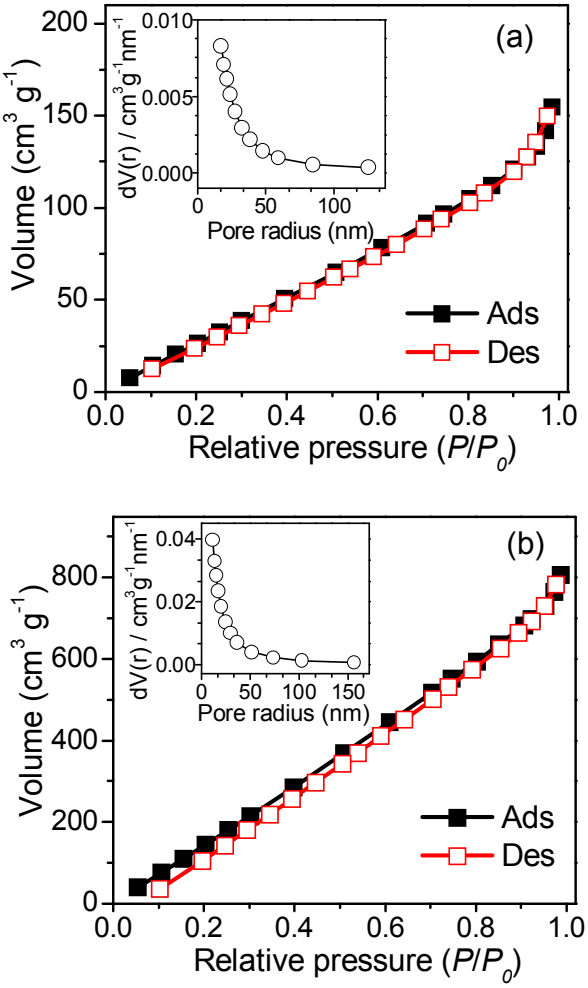

Fig. 3. By L. Yin, D. Chen, and *et al.*.

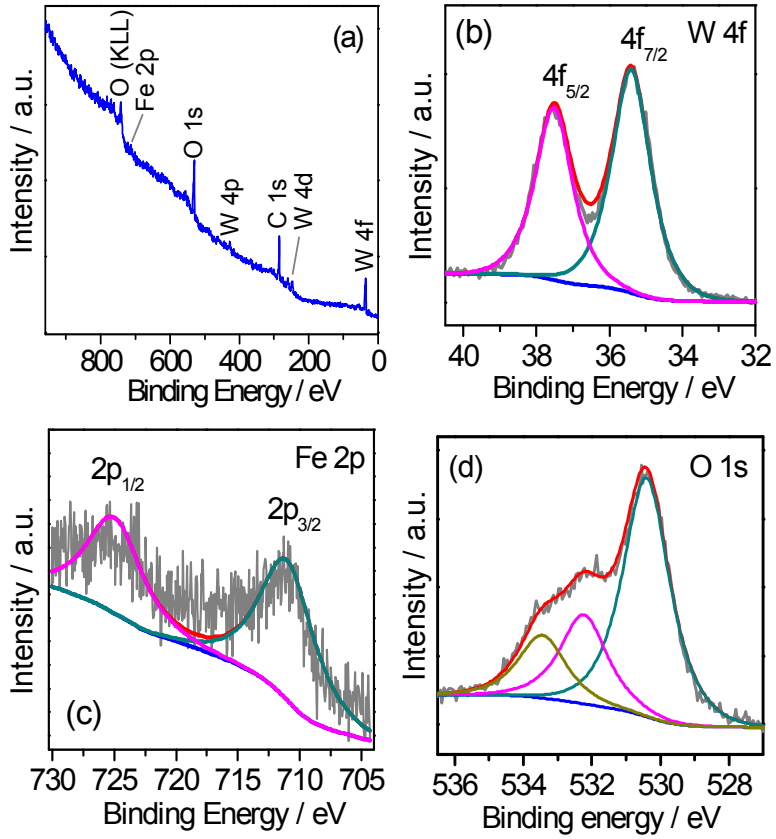

Fig. 4. By L. Yin, D. Chen, and *et al.*.

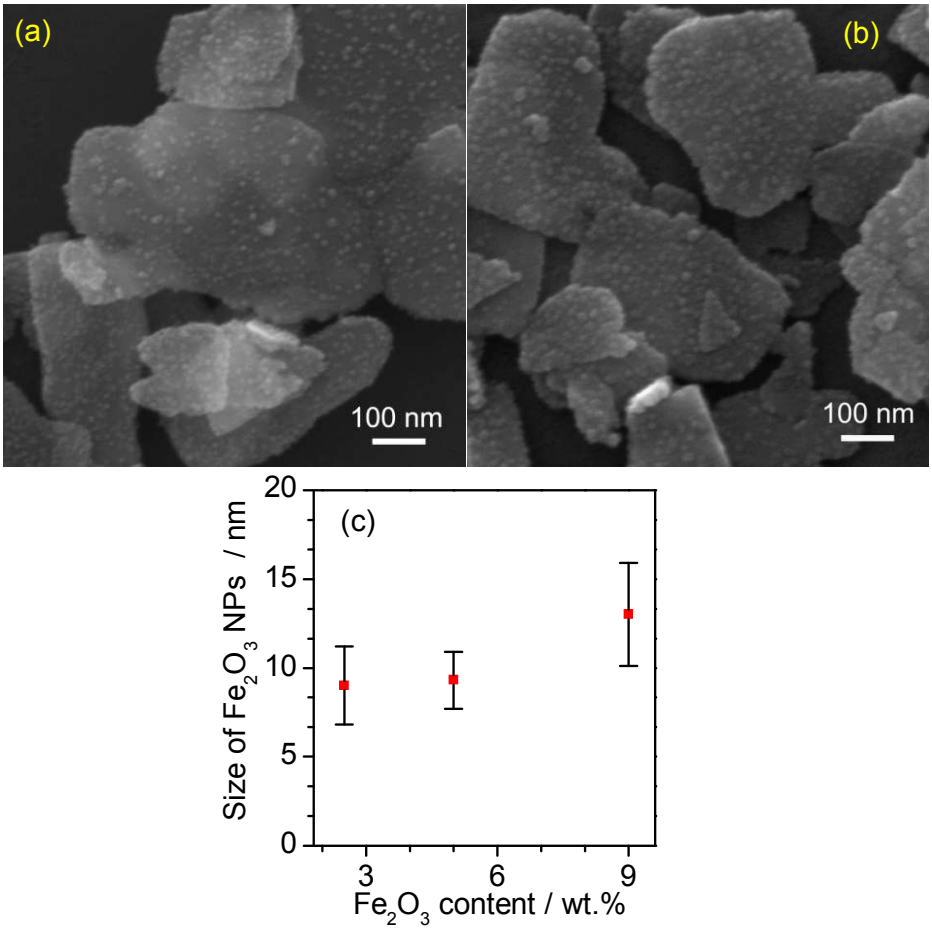

Fig. 5. By L. Yin, D. Chen, and *et al.*.

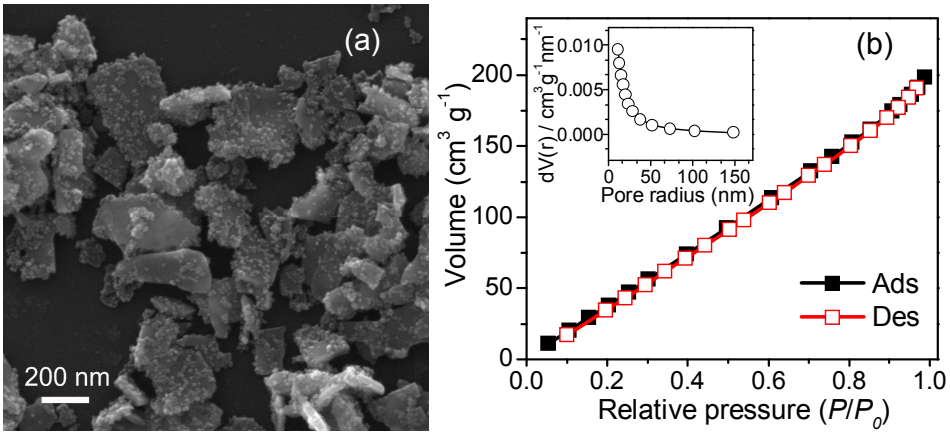

Fig. 6. By L. Yin, D. Chen, and *et al.*.

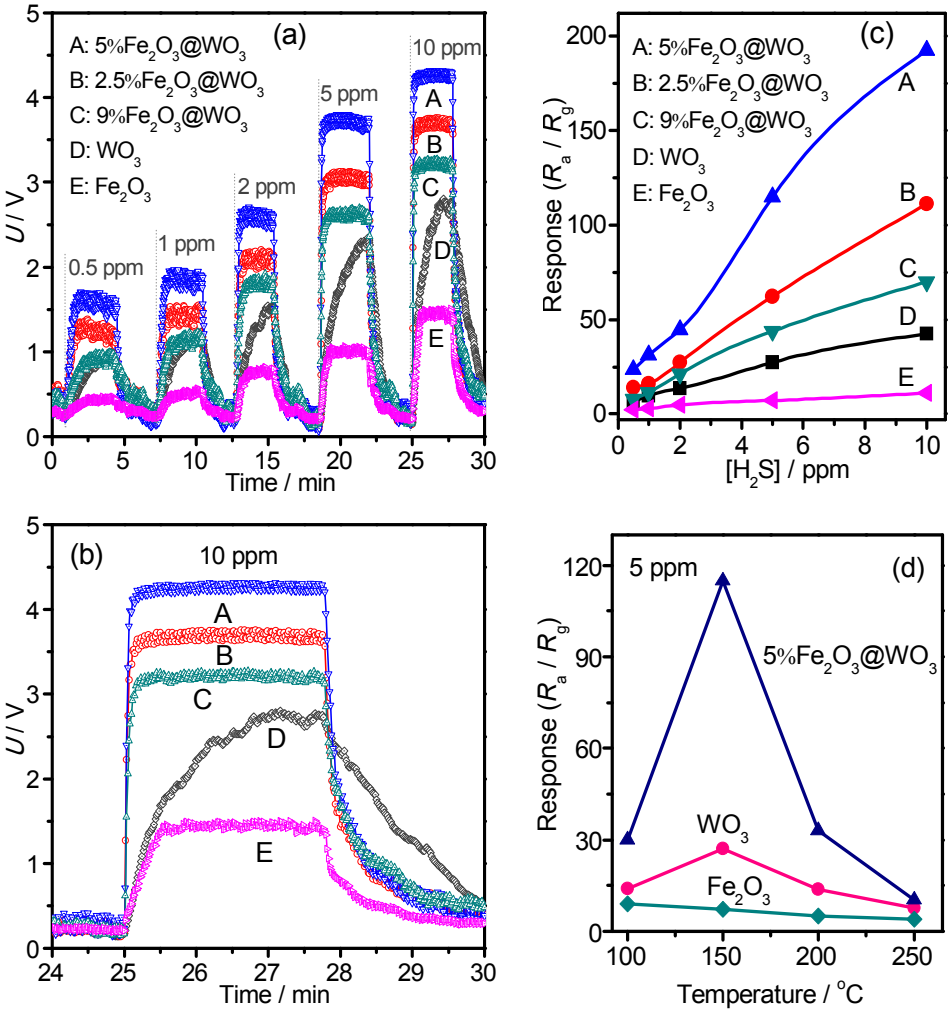

Fig. 7. By L. Yin, D. Chen, and *et al.*.

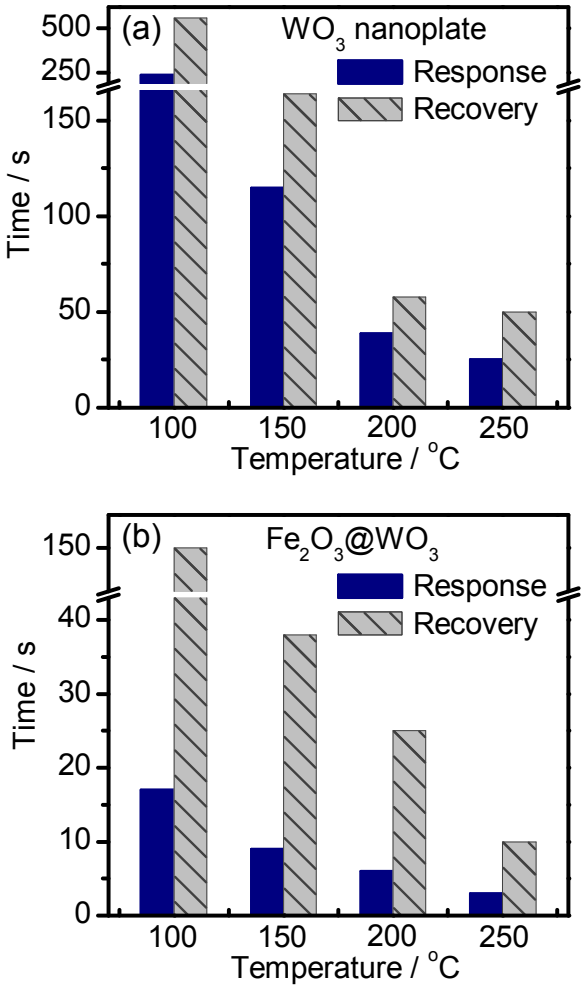

Fig. 8. By L. Yin, D. Chen, and *et al.*.

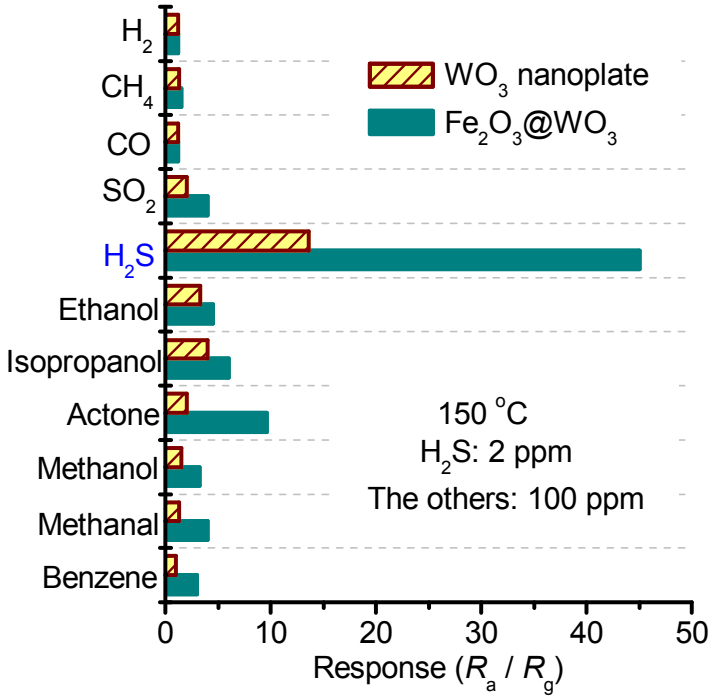

Fig. 9. By L. Yin, D. Chen, and *et al.*.

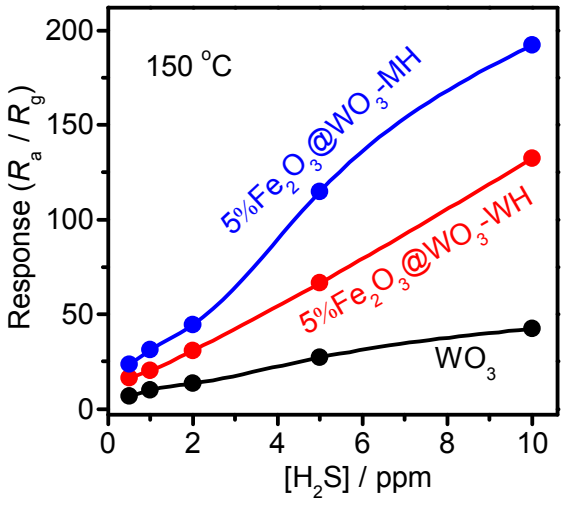

Fig. 10. By L. Yin, D. Chen, and *et al.*.

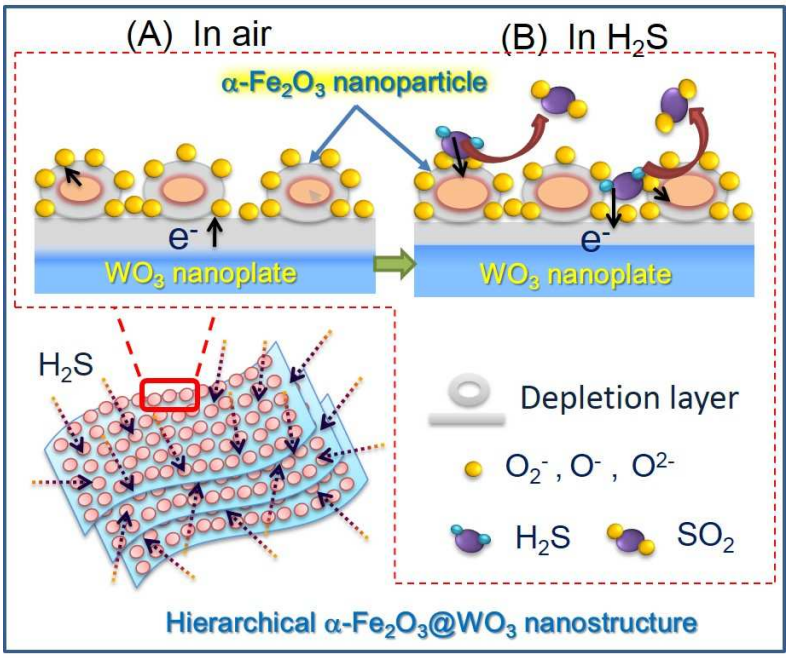

Fig. 11. By L. Yin, D. Chen, and *et al.*.